Zeitschrift: Helvetica Physica Acta

Band: 58 (1985)

Heft: 1

Artikel: The use of EPR spectroscopy and crystal-field parameters to characterize high-level nuclear waste forms

Autor: Rappaz, Michel

DOI: https://doi.org/10.5169/seals-115578

Helvetica Physica Acta
Vol. 58 (1985) 15-41

0018-0238/85/010015-27$1.50+0.20/0

THE USE OF EPR SPECTROSCOPY AND CRYSTAL-FIELD PARAMETERS TO CHARACTERIZE HIGH-LEVEL NUCLEAR WASTE FORMS

Michel Rappaz

Laboratoire de Métallurgie Physique, Département des Matériaux, Ecole Polytechnique Fédérale de Lausanne, CH-1007 Lausanne, (Switzerland).

ABSTRACT

The basic concept of high level nuclear waste forms is to incorporate radioactive ions in an inert matrice. Monazite, a monoclinic rare-earth orthophosphate, and xenotime, an yttrium orthophosphate with the tetragonal structure of zircon, would be ideal primary containers for the long-lived actinide isotopes. These two systems also provide very good examples of the application of EPR spectroscopy to solid-state chemistry problems. After briefly introducing the spin-hamiltonian formalism used for impurities placed in a crystalline electric field, EPR spectra of intentionally doped orthophosphate powders and single-crystals are presented. With these examples, it is shown that EPR is a very useful technique to identify the type, the valence state and especially the crystallographic site of impurities in crystalline hosts.

1. INTRODUCTION

This lecture does not aim at presenting the latest technical developments or a comprehensive view of the theoretical foundations of Electron Paramagnetic Resonance (EPR). It is oriented towards non-specialized physicists or material scientists who want to know the possibilities offered by this technique in characterizing crystalline systems. For those readers who are interested in specific theoretical or experimental aspects, one shall refer to the books listed in the references section (1 - 9).

After a short introduction to EPR spectroscopy, the spin-hamiltonian formalism used to interpret experimental spectra will be outlined. A few examples will then be provided by the application of this technique to the characterization of high-level nuclear waste forms.

2. BASIC PRINCIPLE OF EPR SPECTROSCOPY

2.1. Preliminary

The basic principle of EPR spectroscopy is the same as that already presented in this lectures series for NMR (10). If nuclear magnetic resonance deals with nuclear magnetic moments, EPR can be applied to atoms or ions possessing an electronic magnetic moment. The number of electrons for a given ion being directly influenced by the chemical bounds with neighbouring atoms, identification of impurities with EPR may not be as simple as with NMR. Similarly, intensity measurement of EPR signals may not reflect the real impurity concentration in a given solid if more than one valence state or crystallographic site are present.

However, EPR spectroscopy is a very powerful, site-specific technique for the study of impurities or defects in solids. It has been applied so far to: i) ions of the transition series (eg. Mn^{2+}, Fe^{3+}, Gd^{3+}, Mo^{5+}, etc.) or atoms (eg. H°, Li°, Ag°, etc.) diluted in diamagnetic matrices; ii) defects in insulating crystals or in semiconductors (e.g. F center); iii) free electrons of metals; iv) ferro- or antiferromagnets; v) free radicals in organic substances.

This lecture will be primarily concerned with paramagnetic impurities (ions or atoms) diluted in solids (insulating crystals or semiconductors).

2.2. EPR of free ions

Let us consider the basic ground state $|LSJM_J\rangle$ associated with the unfilled shell of a paramagnetic ion. The three quantum numbers L, S and J characterizing respectively the angular momentum, the spin and the total momentum of the shell are given by Hund's rules which state that the ground state corresponds to: first, a spin $\vec{S}$ maximum, second an angular momentum $\vec{L}$ maximum (but respecting Pauli's exclusion principle) and finally a total momentum $\vec{J}$ maximum or minimum depending if the shell is more or less than half-filled, respectively. (M_J is the projection of $\vec{J}$ along a z-axis).

When the ion is placed in an external magnetic field $\vec{H}$, the (2J + 1) degeneracy of the ground-state is lifted by the Zeeman term:

$$\mathcal{H}_z = g_J \beta \vec{H} \cdot \vec{J} \tag{1}$$

β is the Bohr magneton (= $9.2741.10^{-24}$ Am^2) and g_J the Landé factor which relates the total magnetic moment $\vec{\mu}_J$ to the momentum $\vec{J}$:

$$g_J = \frac{3}{2} + \frac{S(S+1) - L(L+1)}{2J(J+1)} \tag{2}$$

If photons of appropriate frequency ν are now applied to the ion, transitions can be induced between $|LSJM_J\rangle$ and $|LSJM_J \pm 1\rangle$ states. The resonance condition can be written as:

$$h\nu = E_{M_J} - E_{M_J - 1} = g_J \beta H M_J - g_J \beta H (M_J - 1) = g_J \beta H \tag{3}$$

It should be noticed that, although (2J+1) levels are involved, the 2J transitions between them do have the same resonance condition and thus are superimposed. This will no longer be the case when the ion is placed in a crystalline electric field.

Since it is difficult to vary the photon frequency in an EPR experiment, the resonance condition is matched by varying the amplitude of the external magnetic field. The Bohr magneton β being about 1860 times larger than the nuclear magneton, the resonance frequencies of EPR and NMR are also in the same ratio for a given magnetic field. Accordingly, if NMR uses radio-frequencies (MHz), EPR transitions are induced by microwaves (ν > GHz) for practical magnetic fields (H > k Gauss). Experimental set-up are thus quite different, even through basic principles of NMR and EPR are the same.

3. SPIN HAMILTONIAN AND CRYSTAL-FIELD PARAMETERS

3.1. Preliminary

When a paramagnetic ion is placed in a diamagnetic crystal, the electric charges of the surrounding ions influence the orbital motion of its electrons. Therefore, its orbital and resulting momentum will be perturbed.

In a point-charge model where no covalency effects are exhibited, the crystal-field term can be written as:

$$V_c = \frac{1}{4\pi\varepsilon_o} \sum_i \sum_\alpha - \frac{q_\alpha \cdot e_i}{|\vec{r}_i - \vec{r}_\alpha|} \qquad (4)$$

where the summations i and α are carried out for the electrons of the paramagnetic ion and the surrounding charges q_α, respectively.

In order to calculate the effect of V_c on the paramagnetic ion states, one should consider 3 different cases:

- Weak crystal-field: if V_c is much smaller than the spin-orbit coupling, the ground-state given by Hund's rules is a good starting point and the influence of V_c on $\vec{J}$ may be calculated.

- Intermediate crystal-field: when V_c is greater than but comparable to the

spin-orbit coupling, one must first consider the action of V_c on the orbital momentum $\vec{L}$, then the $\vec{L}$-$\vec{S}$ coupling.

- Strong crystal-field: for V_c much stronger than the spin-orbit coupling, individual electronic contributions have to be calculated.

As it can be seen, the problem is not simple ! However, one should remember that EPR measures only the lowest electronic levels in a cm^{-1} range or so. Therefore, experimental EPR spectra are usually described with a spin Hamiltonian where an effective spin $\tilde{S}$ is introduced. In the case of very weak crystal fields where all the $|LSJM_J>$ levels of the free-ion ground state will be 'seen' in EPR experiments, $\tilde{S}$ is simply equal to $\vec{J}$. In more complicated cases, $\tilde{S}$ is chosen in such a way that $(2\tilde{S}+1)$ describes the number of levels involved in the resonance. For example, if only one EPR line is observed, one takes $\tilde{S} = 1/2$ (doublet).

In the following, $\tilde{S}$ will be simply labeled $\vec{S}$ accordingly to most textbooks. Although this may be confusing, it has some physical meaning for S-state ions such as Mn^{2+}, Fe^{3+}, Gd^{3+}, Pb^{3+}, etc. For such cases, the ground state is characterized by L = 0 and one has effectively $\tilde{S} = S = J$.

3.2. Spin Hamiltonian

If a single resonance line is observed, it is sufficient to take the effective spin as $S = \frac{1}{2}$. The behaviour of this line may be described by the following hamiltonian:

$$\mathcal{H} = \beta \vec{H}.\overleftrightarrow{g}.\vec{S} \qquad (5)$$

where $\overleftrightarrow{g}$ is a tensor reflecting the symmetry of V_c. In a principal axes system where $\overleftrightarrow{g}$ has a diagonal form, eqn. 5 can be written as:

$$\mathcal{H} = H\beta(kg_xS_x + lg_yS_y + mg_zS_z) \qquad (5')$$

(k, l, m) are the three director cosines of the magnetic field $\vec{H}$. It is easy to show that the position of the EPR line is given by an equation similar to eqn. 3:

$$h\nu = g\beta H \tag{6}$$

However, g is no longer the Landé factor and its value is usually angular-dependant:

$$g^2 = g_x^2 k^2 + g_y^2 l^2 + g_z^2 m^2 \tag{7}$$

The principal values (g_x, g_y, g_z) are deduced from special orientations of the magnetic-field. An example of axial symmetry ($g_x = g_y = g_\perp$; $g_z = g_\parallel$) is given in section 4.

If more than one EPR line is observed, additional fine structure terms have to be added to eqn. 5.

$$\mathcal{H} = \beta \vec{H} \overleftrightarrow{g} \vec{S} + \sum_{k,q} B_k^q O_k^q \tag{8}$$

The B_k^q's, which are called the crystal-field parameters, are normally deduced from the experimental spectra. They multiply the Stevens Operators O_k^q whose form is dictated by point-symmetry considerations and may be deduced from Wigner-Eckart theorem.

These operators which are k-order expansions of $\vec{S}$ are closely related to the spherical harmonics $Y_k^q(\theta, \phi)$. For example: $Y_2^0(\theta, \phi) = 3\cos^2\theta - 1 \simeq 3z^2 - r^2$ and $O_2^0 = 3S_z^2 - S(S+1)$. This equivalence is not always as simple due to the non-commutation of the components of $\vec{S}$.

The number of terms which have to be considered in eqn. 8 is limited by: first, the symmetry of the crystal-field and second, rules similar to those used when adding momenta. Effectively, the matrix elements $\langle SM_s' | O_k^q | SM_s \rangle$ will be different from zero only if:

$$|S - k| \leq S \leq (S + k) \text{ and } M_s' + q = M_s$$

A few examples in section 4 will illustrate the use of the spin-hamiltonian.

3.3. Spin-hamiltonian parameters

As already explained, the parameters B_k^q as well as the components of the $\overleftrightarrow{g}$ tensor appearing in the spin hamiltonian (Eqn. 8) are normally deduced from the experimental spectra. They are effectively very difficult (if not impossible!) to calculate since they contain the physics of the crystal-field interaction. For a given paramagnetic impurity, these parameters are measured in function of: temperature, pressure, lattice parameter of isostructural host crystals, etc. The B_k^q coefficients are then fitted very frequently to power laws of type ρ^{-n}, where ρ is the nearest-neighbour distance and n an adjustable exponent. The parameter n is often far from the (k+1) value predicted by a point-charge model for various reasons: covalency effects, local lattice distorsions, vibrational effects.

3.4. Hyperfine and superhyperfine interactions

Besides S-state ions with $S \geqslant 3/2$ for which many lines are observed, identification of a paramagnetic impurity from an EPR spectra is not an easy task. Hopefully, these spectra very often carry the signature of the nuclear magnetic moment $\vec{I}$ of one or more isotopes. The hyperfine coupling between $\vec{S}$ and $\vec{I}$ is written as:

$$\mathcal{H}_{hf} = \vec{I}.\overleftrightarrow{A}.\vec{S} \qquad (9)$$

where $\overleftrightarrow{A}$ is the hyperfine tensor whose form is similar to that of $\overleftrightarrow{g}$ but whose principal axes are not necessarily parallel to those of $\overleftrightarrow{g}$.

In the isotropic case $g_x = g_y = g_z = g$ and $A_x = A_y = A_z = A$, it is easy to show that, in first order, the energy levels are given by:

$$E(M_s, M_I) = g\beta HM_s + AM_IM_s$$

Accordingly, the "allowed" electronic transitions $\Delta M_s = \pm 1$ are given by:

$$h\nu = g\beta H + AM_I \tag{10}$$

(2I + 1) lines equidistant in first order and of same intensity will thus be observed around the central g value.

Similarly, the effective spin $\vec{S}$ may interact with the nuclear magnetic moment $\vec{I}_\alpha$ of neighbors α. In this case, the superhyperfine interaction will be a sum:

$$\mathcal{H}_{shf} = \sum_\alpha \vec{S}\, \overleftrightarrow{T}_\alpha . \vec{I}_\alpha \tag{11}$$

The tensor $\overleftrightarrow{T}_\alpha$ has usually an axial symmetry along the bonding direction. When the magnetic field $\vec{H}$ is applied at an angle θ_α to the bond, the EPR transitions associated with this coupling are in first order:

$$h\nu = g\beta H + \sum_\alpha T_\alpha(\theta_\alpha) M_\alpha \tag{12}$$

with

$$T_\alpha(\theta_\alpha) = \sqrt{T_{\parallel\alpha}^2 \cos^2\theta_\alpha + T_{\perp\alpha}^2 \sin^2\theta_\alpha}$$

$T_{\parallel\alpha}$ and $T_{\perp\alpha}$ are the superhyperfine "constants" parallel, respectively perpendicular, to the bond between the paramagnetic ion and the neighbour α.

4. CHARACTERIZATION OF HIGH-LEVEL NUCLEAR WASTE FORMS BY EPR SPECTROSCOPY

4.1. Preliminary

In an approach to the containment of nuclear waste in which the primary waste form is a crystalline substance, the basic concept is to incorporate radioactive ions in an inert crystal lattice. Ideally, these ions

would occupy substitutional sites that are normally occupied by ions of the host material. Borro-silicate glasses have been extensively studied and are considered as a good potential candidate since they can be produced at low temperature and at low cost. However, these glasses have been found to be unstable under certain hydrothermal conditions. For that reason, alternate nuclear waste forms such as ceramics or crystalline systems have also been considered (11).

EPR spectroscopy yields the maximum amount of information when applied to this type of solid-state situation, i.e. to paramagnetic impurities diluted in a crystalline system. It should be noted, however, that this technique has been also applied to investigations of impurities or defects in glasses and thus it is not limited to crystalline substances.

4.2. High-level waste composition

Table 1 gives the composition of a standard commercial high-level waste which is obtained after processing of the nuclear fuel burnt in a reactor. For each element is listed: its molar concentration, the most common chemical

Table 1. PW-4b nuclear waste composition and valence states.

	MOL %	VALENCE	DETECTED BY EPR		MOL %	VALENCE	DETECTED BY EPR
La		+3	+2	Pd	4.1	+2, +4	+3
Ce		+3, +4	+3	Sr	3.5	+2	
Pr		+3, +4	+3	Ba	3.5	+2	
Nd		+3	+3, +4	Rb	1.3	+1	
Pm		+3	+3	U	1.4	+3 - +6	+3, +4, +5
Sm		+2, +3	+3	Th		+4	
Eu		+2, +3	+2	Np	0.2	+3 - +6	+4, +6
Gd	26.4	+3	+3	Pu		+3 - +6	+3, +6
Tb		+3, +4	+3, +4	Am		+3 - +6	+2, +4
Dy		+3	+3	Cm		+3	+3
Ho		+3	+2, +3	Fe	6.4	+2, +3	+1, +2, +3
Er		+3	+3	Na	1.0	+1	
Tm		+2, +3	+2	PO_4	3.2		
Yb		+2, +3	+3	Tc	9.0	+7	+4
Lu		+3		Rh		+2, +3, +4	+2
Zr	13.2	+4		Te		-2, +4, +6	
Mo	12.2	+6 - +2	+3, +5	In		+3	+2
Ru	7.6	+2, +3, +4 +6, +8	+3	Ni		+2, +3	+1, +2, +3
Cs	7.0	+1		Cr		+2, +3, +6	+3, +5 (+4) +1 (+2)

valence states as found in a periodic table, and the valence states for which an EPR spectrum has been reported in the literature (12). A few observations can be made: i) one fourth of the elements are rare-earths which have interesting magnetic properties, while Zr and Mo are another fourth; ii) Fe which is also an interesting element for EPR is at relatively low concentration (6.4%) in commercial waste. However, in defense waste, it can amount to more than 50%; iii) besides alcaline and alcaline-earth elements, almost all elements have been observed by EPR.

4.3. Monazite and xenotime as waste forms

Monazite, a cerium orthophosphate ($CePO_4$) with a monoclinic structure, and xenotime, an yttrium orthophosphate (YPO_4) with the tetragonal structure of zircon, are two minerals found in nature. They have interesting characteristics for the containment of nuclear wastes (13),: i) chemical stability; ii) natural high concentration of uranium and thorium (up to 16%); iii) strong resistance against α-radiations since they never exhibit a metamict structure; and iv) very low solubility in water and a negative temperature coefficient of solubility.

In view of these desirable characteristics, a series of investigations of the physical and chemical properties of natural monazite, xenotime and the related, synthetically produced lanthanide* orthophosphates has been undertaken. Some of the EPR results which illustrate the use of the spin-hamiltonian formalism in characterizing paramagnetic impurities in solids are presented in the next paragraph.

4.4. EPR spectra of impurities in $LnPO_4$

4.4.1. Pb^{3+} in xenotime-type orthophosphates (14)

Let start with a simple ion. Lead, whose chemical valences are normally +2 or +4, is incorporated in the zircon-type YPO_4 and $LuPO_4$ hosts

*Yttrium and scandium will be associated with the rare-earths since they have closely related chemical properties.

in a 3+ valence state. Its electronic configuration being $6S^1$, the associated ground-state is $^2S_{\frac{1}{2}}$ (The standard notation is adopted here: $^{(2S+1)}L_J$). Since L = 0, this is an S-state ion and furthermore S = J = ½. Therefore, only one line is observed near g = 2 in Fig. 1. The central transitions of Fe^{3+} and Gd^{3+} which are clearly visible on this figure have been labeled. The Pb^{3+} signal exhibit a typical superhyperfine structure: the five lines whose intensities are in the ratio 1:4:6:4:1 are due to the various combinations of the nuclear momentum of 4 equivalent ^{31}P second-neighbours ($I(^{31}P) = \frac{1}{2}$). Since they are equivalent for this orientation of the magnetic field ($\vec{H} \parallel c$, where c is the axis of the tetragonal structure), the values $T_\alpha(\theta_\alpha)$ in eqn. 12 may be taken out of the summation. Thus, the resonance condition becomes:

$$h\nu = g\beta H + T \sum_{\alpha=1}^{4} M_\alpha \qquad \text{with } M_\alpha = \pm \frac{1}{2}$$

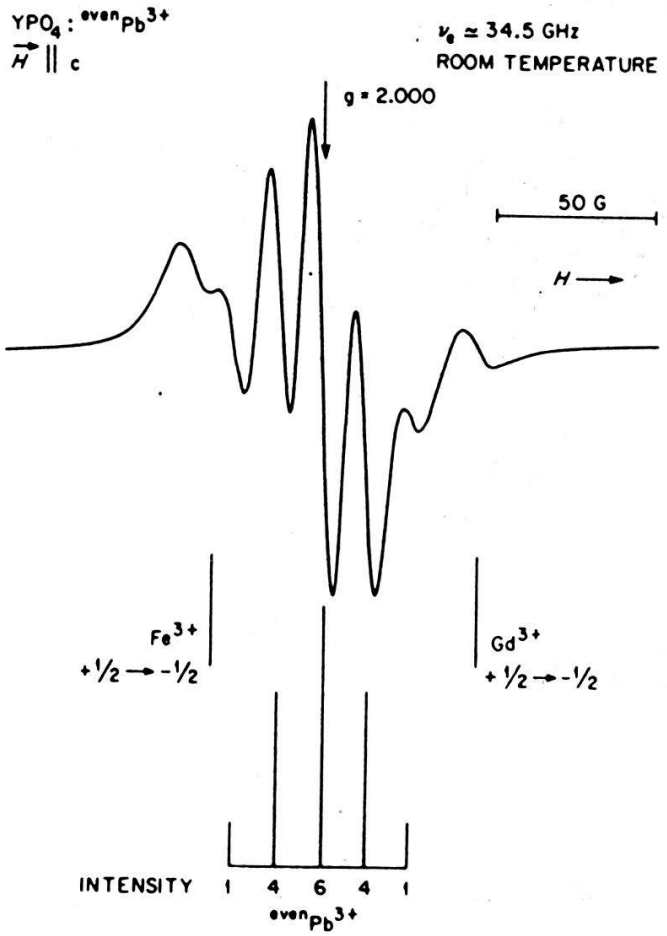

Fig. 1. $-\frac{1}{2} - +\frac{1}{2}$ EPR transition of even Pb^{3+} isotopes in a xenotime single-crystal. The magnetic field is parallel to the c-axis.

This explains the number and intensity of the lines observed for Pb^{3+} in Fig. 1.

If the superhyperfine coupling permits in this case to identify the site occupied by the impurity as that of Ln^{3+}, the positive identification of Pb^{3+} was made possible by the isotope ^{207}Pb (natural abondance ~ 20%). This isotope is characterized by a nuclear momentum $I = \frac{1}{2}$ which interacts strongly with the electronic spin $S = \frac{1}{2}$. For the "free" ion (i.e. ion not incorporated in a matrix), the hyperfine constant is 2.6 cm^{-1}. Since A is large, the first-order calculation made in the previous section is no longer valid and one has to diagonalize $\langle M'_s m'_I | \mathcal{H} | M_s m_I \rangle$ exactly in order to find the energy levels shown in Fig. 2. The levels have been computed with the A-value measured in YPO_4

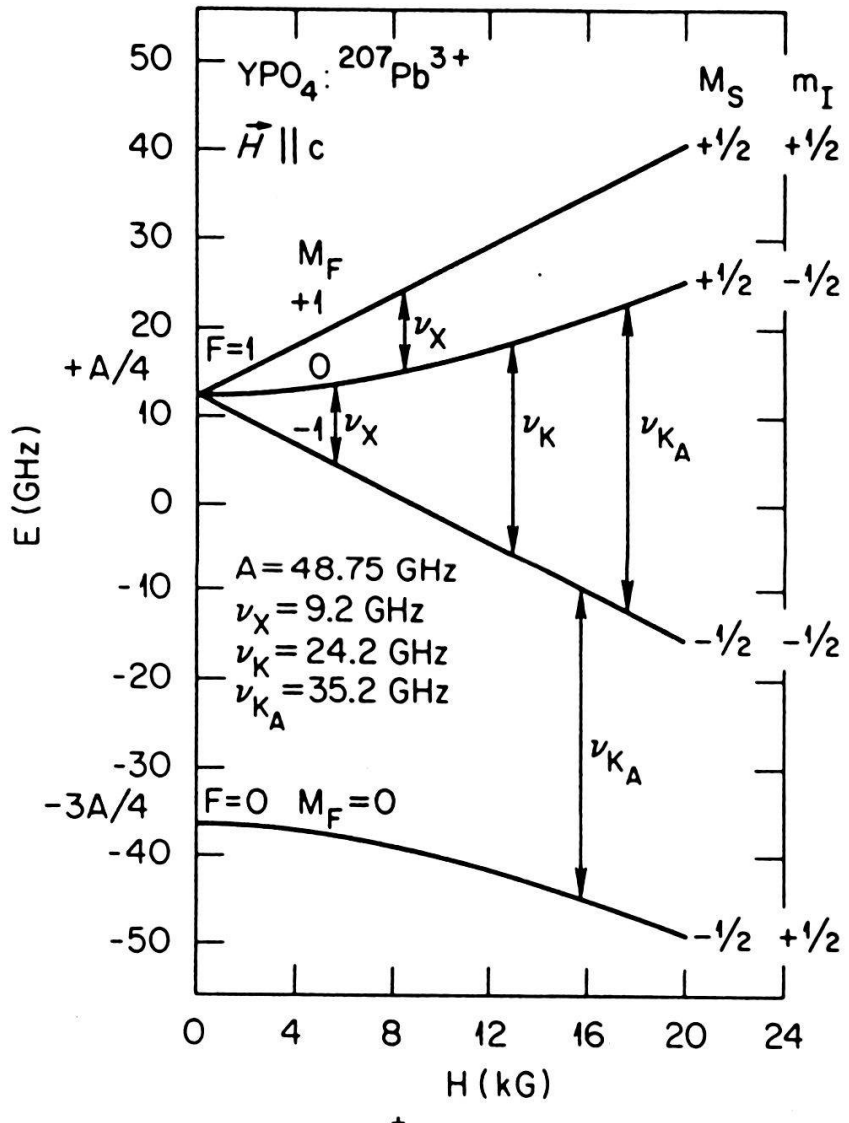

Fig. 2. Energy levels of $^{207}Pb^{3+}$ ($S = I = \frac{1}{2}$) in xenotime.

($\sim$ 1.6 cm^{-1}) and in function of the amplitude of the magnetic field H. The transitions which are "allowed" ($\Delta m_I = 0$, $\Delta M_s = \pm 1$) and "forbidden" ($\Delta m_I = \pm 1$, $\Delta M_s = 0$) are indicated by arrows for various microwave frequencies. Fig. 3 shows the behaviour of the two transitions observed at K_A band ($\nu \simeq 35$ GHz). When increasing the frequency from spectra (a) to (f), the allowed transition position increases in magnetic field while the forbidden transition moves to lower fields as expected from the energy diagram shown in

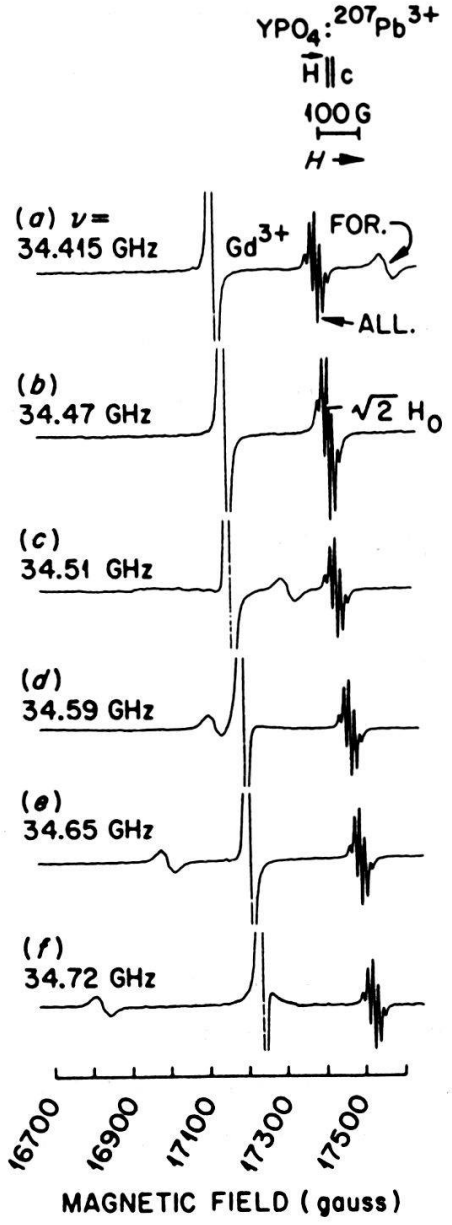

Fig. 3. High-field EPR transitions of $^{207}Pb^{3+}$ in xenotime. As the microwave frequency is increased from a to f, the allowed transition moves at higher fields while the forbidden line position decreases.

Fig. 2. One can show that the superposition of the two transitions occurs for a frequency $\nu = A/\sqrt{2}$. It should finally be noted that the allowed transition of $^{207}Pb^{3+}$ exhibits the same superhyperfine structure observed for the even isotopes (Fig. 1), while this interaction is not resolved for the forbidden transition (larger linewidths).

4.4.2. Fe^{3+} in xenotime-type crystals (15)

The 3+ valence state of iron corresponds also to an S-state (L = 0) but with J = S = 5/2 in that case since Fe^{3+} has 5 electrons on the 3d shell. In a tetragonal symmetry, the spin-Hamiltonian of Fe^{3+} is the following:

$$\mathcal{H} = \beta \vec{H} \overleftrightarrow{g} \vec{S} + B^0_2 O^0_2 + B^0_4 O^0_4 + B^4_4 O^4_4$$

The anisotropy of the g value is small ($g_{\parallel} \simeq g_{\perp}$) as well as the non-diagonal term B^4_4. When the magnetic-field is parallel to the c-axis of the crystal, the energy levels of the 5 EPR transitions are given by:

$$\pm 5/2 \longleftrightarrow \pm 3/2 \qquad H = \frac{1}{g\beta}\left(h\nu \mp (4b^0_2 + 4b^0_4)\right)$$

$$\pm 3/2 \longleftrightarrow \pm 1/2 \qquad H = \frac{1}{g\beta}\left(h\nu \mp (2b^0_2 - 5b^0_4)\right)$$

$$1/2 \longleftrightarrow -1/2 \qquad H = \frac{h\nu}{g\beta}$$

with $b^0_2 = 3B^0_2$ and $b^0_4 = 60\ B^0_4$.

The spectrum of Fig. 4a illustrates this situation. (The seven weaker lines are due to unintentional Gd^{3+} impurities). When the magnetic-field $\vec{H}$ is rotated in the a-c plane, the 5 lines move: their position in function of the rotation angle is plotted in Fig. 5. For $\vec{H} \perp c$, one obtains the EPR spectrum shown in Fig. 4b.

The results shown in Figs. 4a, b and 5 are of course only valid for single-crystals. When similar observations are carried out on powders, the

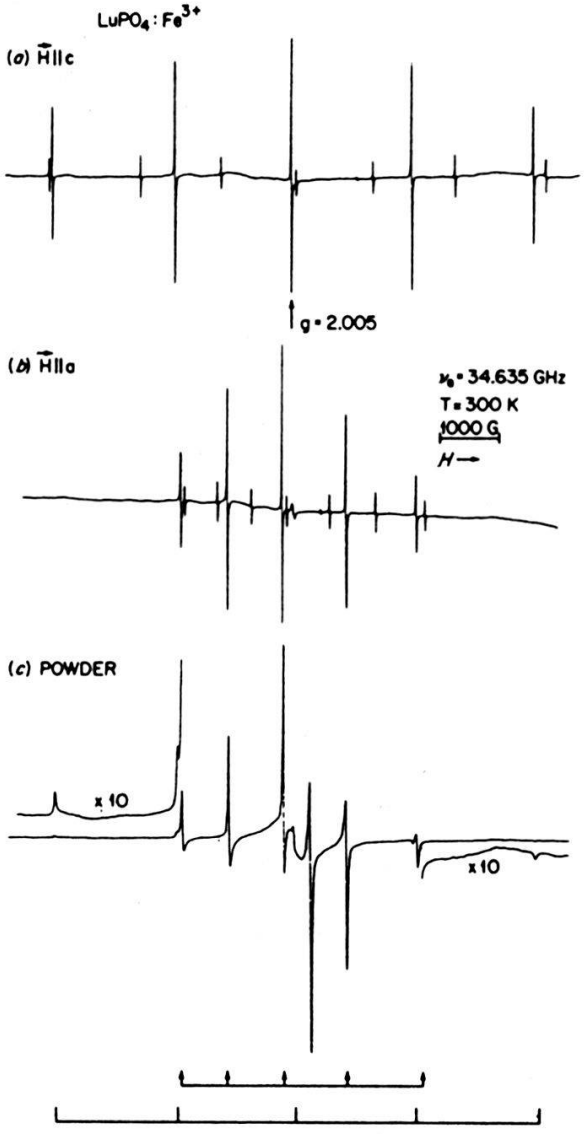

Fig. 4. EPR spectrum of Fe^{3+} ($3d^5$, $^6S_{5/2}$) in $LuPO_4$. a) Single-crystal with $\vec{H} \parallel c$; b) single-crystal with $\vec{H} \perp c$ and c) powder spectrum. Shoulders and divergences are labeled with sticks and arrows, respectively.

intensity of each line has to be averaged between the extremal positions $H_{\parallel}$ and $H_{\perp}$ (i.e. corresponding to the single-crystal line position when $\vec{H}$ is parallel, respectively perpendicular, to the c-axis). One can show that this average results in a shoulder (finite intensity) at $H_{\parallel}$ and a divergence at $H_{\perp}$ (intensity diverging as $(H - H_{\perp})^{-\frac{1}{2}}$). This explains the shape of the first-derivative powder spectrum shown in Fig. 4c. A comparison with the single-crystal spectra shown in a and b clearly indicates that the Fe substitutional sites in powders prepared by a technique of coprecipitation in molten urea (16) are identical to those in flux-grown single-crystals.

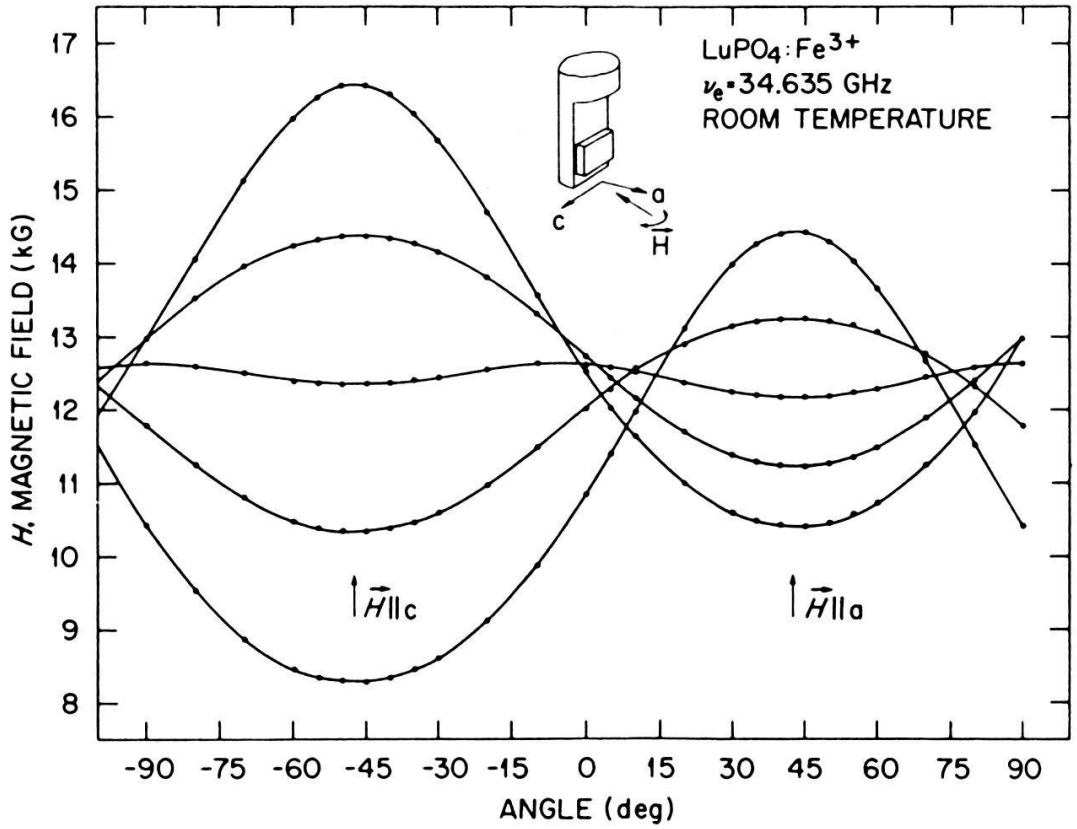

Fig. 5. Angular variation of the 5 EPR lines of Fe^{3+} in $LuPO_4$. Spectra in Figs. 4a and 4b correspond to the orientation labeled with $\vec{H} \parallel c$ and $\vec{H} \parallel a$. The powder spectrum shown in Fig. 4c can be obtained by a proper average of this angular variation.

Furthermore, the intensity of the Fe^{3+} lines as compared to those of unintentional Gd^{3+} impurities revealed that iron is not easily incorporated in these hosts due to its small ionic radii. It is mostly segregated in the lead flux used to prepare the crystals. In powders, similar conclusions were reached as indicated in Fig. 6. In a, the EPR spectrum directly measured after precipitation and calcination at 800 ^{o}C exhibits a broad line due to Fe aggregates, superimposed to the weaker lines of those impurities already incorporated in the lattice. Annealing and quenching the specimen (Fig. 6b) increase considerably the concentration of substitutionel Fe^{3+} impurities while decreasing the central line.

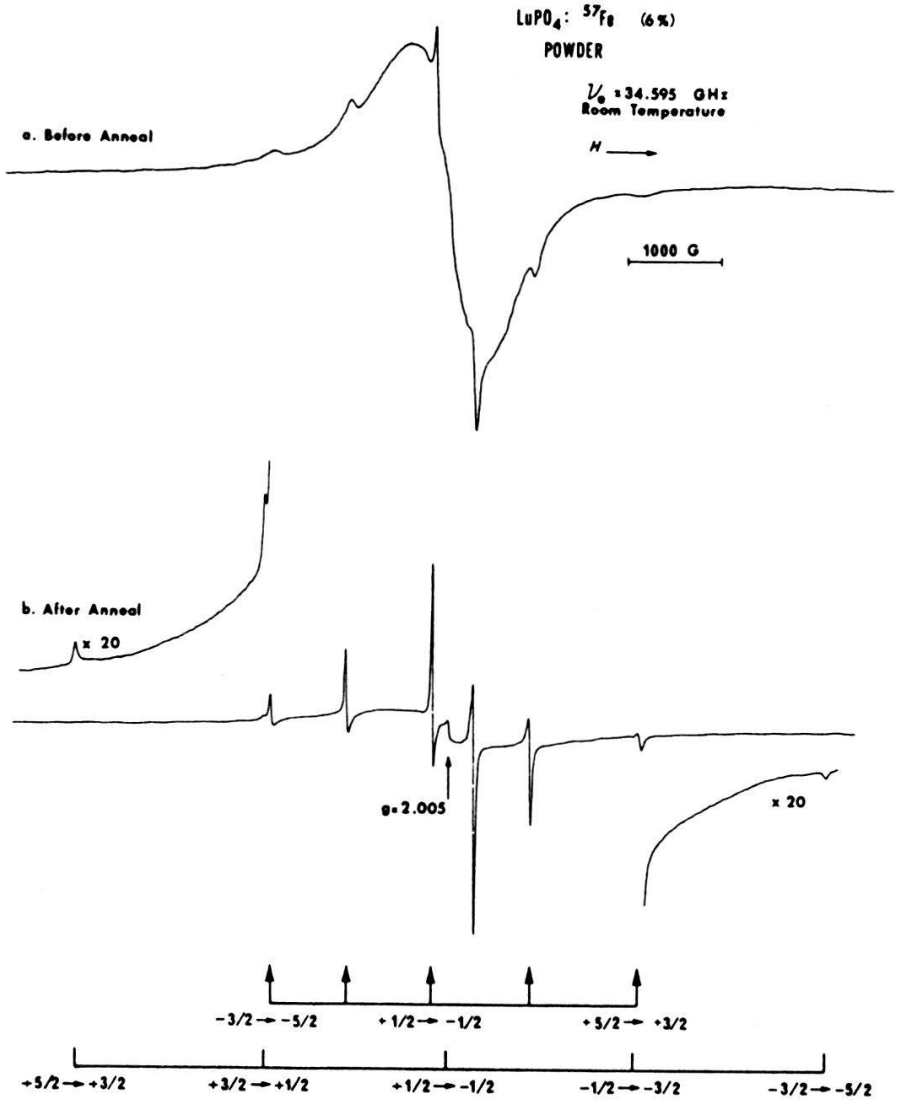

Fig. 6. EPR powder spectra of Fe^{3+} in $LuPO_4$. a) after coprecipitation in molten urea and calcination at 800 °C; b) after annealing in a torch and quenching.

4.4.3. Gd^{3+} in orthophosphates (17, 18)

Gd^{3+} impurities were extensively studied in both the tetragonal- (17) and the monoclinic-type (18) orthophosphates. The first results will not be presented here since they are very similar to those obtained for Fe^{3+} except that seven lines are observed in that case instead of five (Gd^{3+}, $4f^7$ configuration, S = J = 7/2 and L = 0 ground state).

In the monazite-type crystals, precise EPR measurements are not very easy for various reasons. First, the external facets of the crystals do no longer correspond to simple crystallographic planes. Second, the principal electric-field axes do not coincide with those of the crystallographic structure, and third they are 4 rare-earth sites in the unit cell. These 4 sites which are shown in Fig. 7 are equivalent from a crystallographic point of view; they can all be deduced from site 1 with the symmetry operations listed at bottom. Since magnetic-resonance does not distinguish an inversion symmetry, sites 1 and 4 are magnetically equivalent as well as sites 2 and 3. Accordingly, two sets of 7 lines should be observed for an arbitrary orientation of the magnetic field $\vec{H}$. The operation transforming sites (1 - 4) into sites (2 - 3) being a 180-rotation along the b-axis of the structure, the four sites

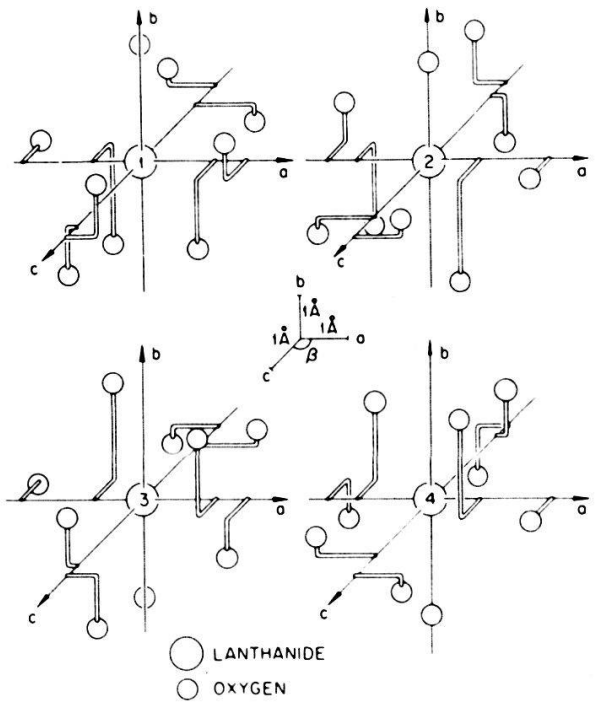

SITE	SYMMETRY OPERATION TO TRANSFORM (Ln_1 SITE) → (Ln_x SITE)
Ln_2	180° ROTATION ABOUT THE b AXIS
Ln_3	REFLECTION ABOUT THE (010) PLANE
Ln_4	INVERSION

Fig. 7. Position of the 9 nearest-neighbours O ions surrounding the 4 rare-earth sites in the unit cell of monazite. The symmetries which transform site 1 into the three others are listed below.

are magnetically equivalent (only 7 lines observed) when $\vec{H}$ is either parallel or perpendicular to b. This equivalence is shown in Fig. 8 for a single-crystal of $LaPO_4$ doped with Gd^{3+}. The position of the 7 lines has been measured for various orientations of the magnetic field in the plane perpendicular to the b-axis. Due to a small misalignment of the crystal, one can see for some orientations that each line is in fact a superimposition of two lines.

The spin-Hamiltonian of Gd^{3+} in such monazite crystals has the following form:

$$\mathcal{H} = \beta \vec{H} \overleftrightarrow{g} \vec{S} + \sum_{n,m} B_n^m O_n^m \quad \text{with } n = 2,4,6 \text{ and } m = 0,2,4,6, \quad m \leq n$$

When $\vec{H}$ is parallel to the Z principal axis* of one of the sites pair (Z_1 for sites (1 - 4) and Z_2 for sites (2 - 3)), the situation is similar to the spectrum shown in Fig. 4a: the spectrum is composed of 7 almost equidistant lines whose position is given at first-order by the diagonal operators O_2^0, O_4^0 and O_6^0. Thus, when turning the magnetic-field in the (Z_1, b, Z_2) plane, one obtains (Fig. 9): a) At -61^0 from the b-axis, $\vec{H}$ is parallel to Z_1 and the 7 almost-equidistant lines labeled at the top correspond to Gd^{3+} impurities in sites (1 - 4). The other lines correspond to (2 - 3) substitutional ions. b) For $\vec{H} \parallel \vec{b}$, the sites are all equivalent (7 superimposed lines). c) At $+61^0$ from the b-axis, $\vec{H}$ is parallel to Z_2 and the situation is similar to (a) with a permutation of the sites (1 - 4) and (2 - 3). d) For $\vec{H} \perp \vec{b}$, all sites are again equivalent.

Such measurement not only determines the sites occupied by Gd^{3+} impurities but also gives the position of the electric-field axes with respect to the crystallographic ones. The z- and y-axes for the two sets of sites are sketched in Fig. 10.

For powder spectra (Fig. 11), the problem of non-equivalent sites does no longer prevail and it is sufficient to consider only one. The average

---

*The z-axis is defined in that case as the one for which the splitting of the lines is maximum.

of each line in the powder spectrum gives 2 shoulders at magnetic-field values corresponding to $\vec{H} \parallel z$ and $\vec{H} \parallel y$ with a divergence in between whose position is that of the single-crystal line when $\vec{H} \parallel x$. Shoulders and divergences are labeled with sticks and arrows at bottom of Fig. 11.

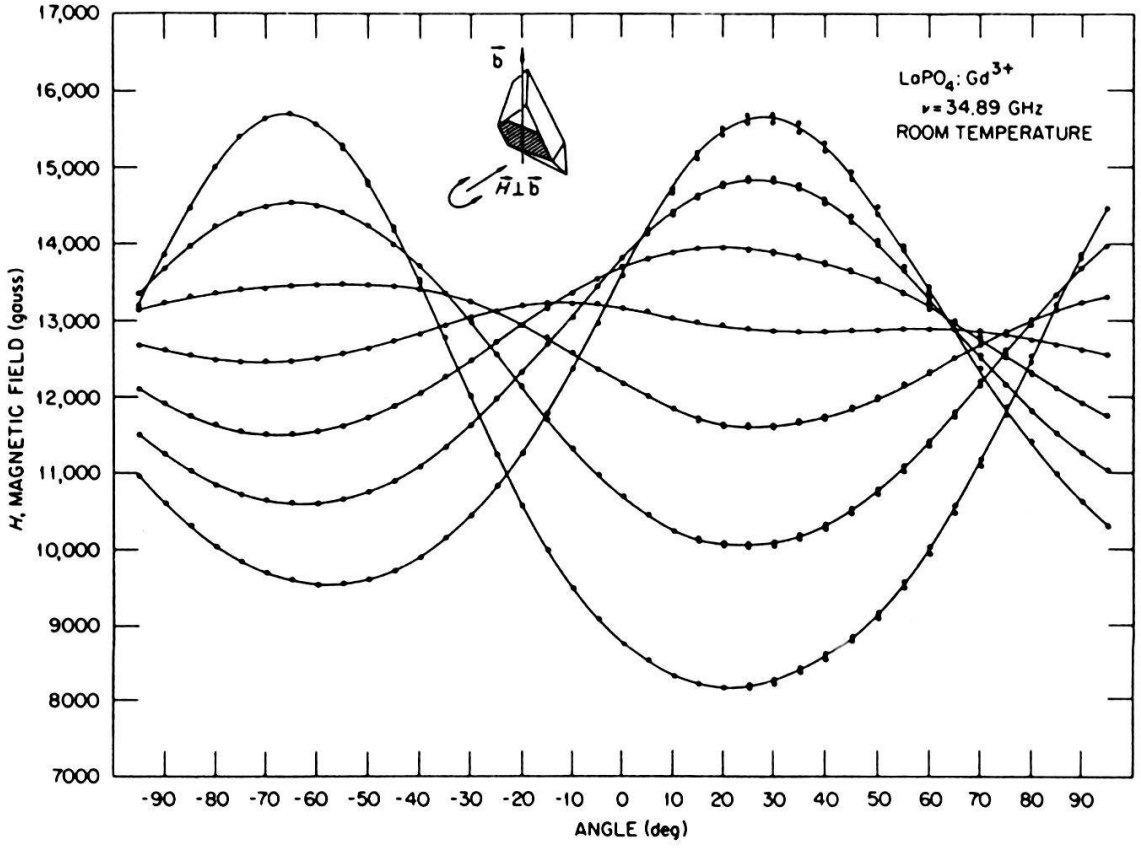

Fig. 8. Angular dependence of the EPR spectrum of Gd^{3+} in monazite-type $LaPO_4$ single crystal with the magnetic field rotated in the plane perpendicular to the b-axis. Each curve is doubly degenerate in this plane.

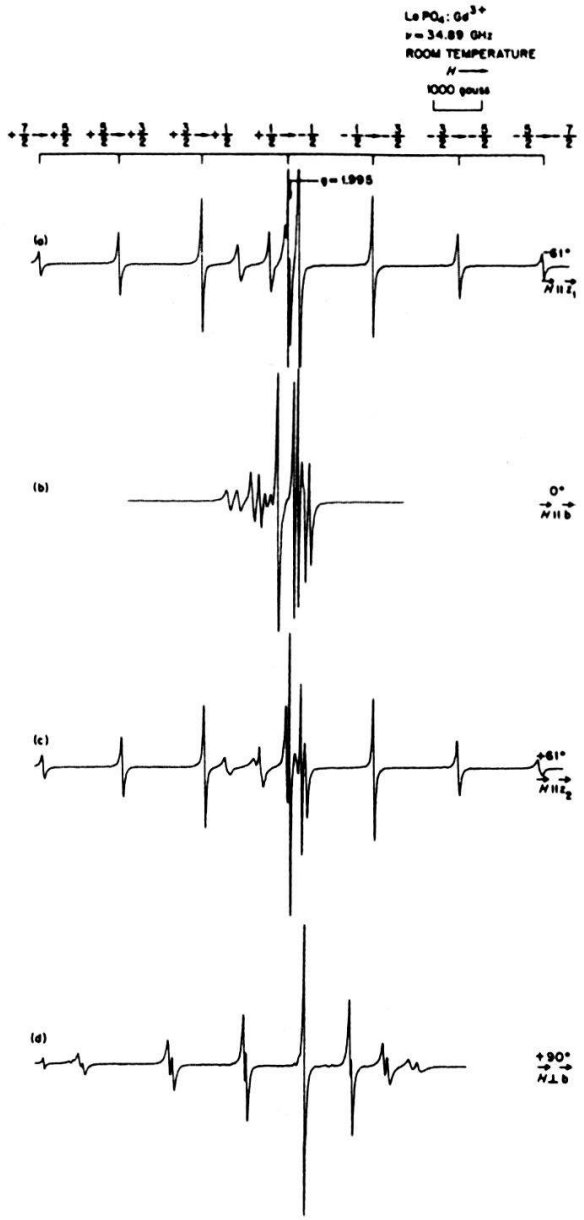

Fig. 9. EPR spectra of Gd^{3+} in monazite-type $LaPO_4$ single-crystal. The magnetic field is rotated in the (Z_1, b, Z_2) plane.

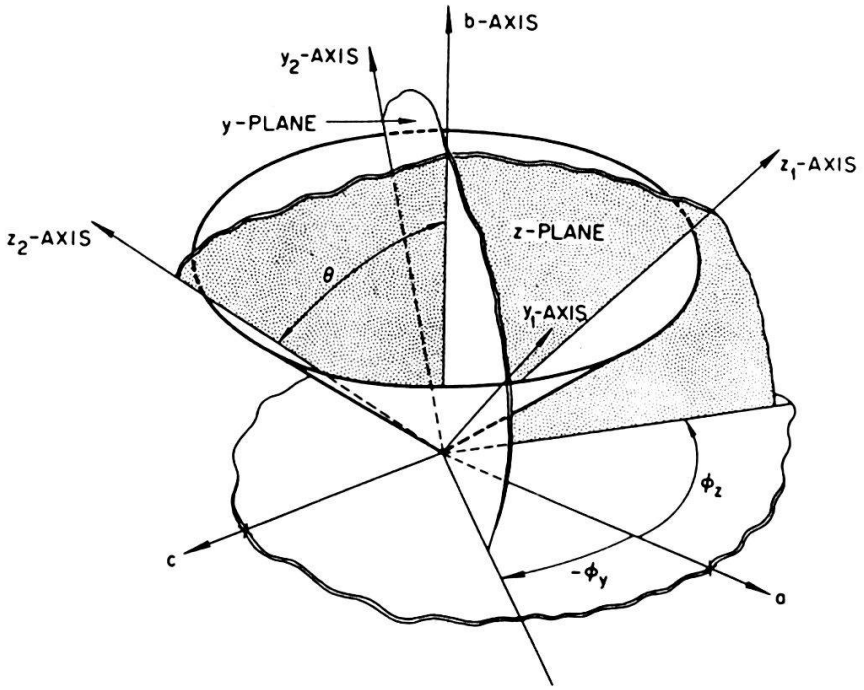

Fig. 10. Orientation of the crystal-field principal axes of Gd^{3+} in monazite-type rare-earth orthophosphates. The z- and y-axis for sites (1 - 4) and (2 - 3) lie on the same cone (e.g. $\theta = 61^{o}$ for $LaPO_4$: Gd^{3+}, Fig. 9).

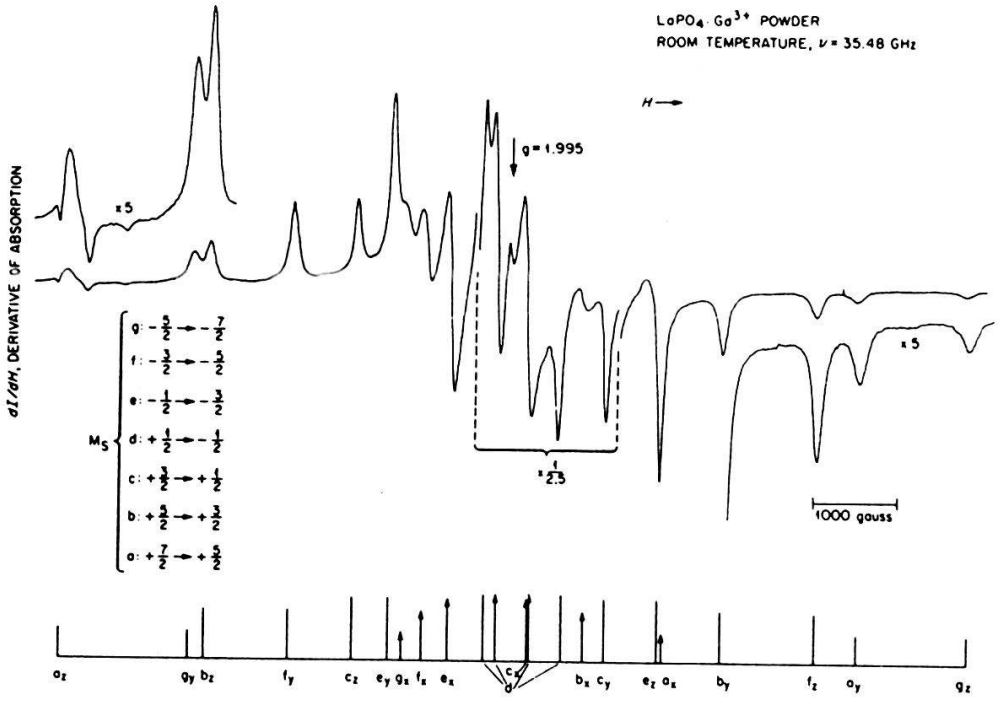

Fig. 11. EPR powder spectrum of $LaPO_4$: Gd^{3+}. Shoulders and divergences are labeled for each transition noted (a) - (g) with sticks and arrows. The central transition $-\frac{1}{2} \leftrightarrow +\frac{1}{2}$ has a complicated lineshape due to second-order terms (18).

4.4.4. Other impurities

In the previous sections, S-state ion EPR spectra have been presented. Other impurities which are not characterized by an L = 0 ground-state have also been measured in the orthophosphate hosts, in particular Zr^{3+} (19), Ln^{3+} (20), Cm^{3+} (21) and U^{3+} (21). In most cases, only one line besides hyperfine or superhyperfine structures was observed.

For U^{3+} ($5f^3$, $^4I_{9/2}$) in $LuPO_4$, the ground state is splitted in 5 doublets by the tetragonal crystal field and one measures only the low-lying one. The position of this line measured by its g-value is reported in Fig. 12 in function of the angle between $\vec{H}$ and the c-axis. Since g can be written as $\sqrt{g_{\parallel}^2 \cos^2\theta + g_{\perp}^2 \sin^2\theta}$ (eqn. 7), $g^2(\cos^2\theta)$ is a straight line.

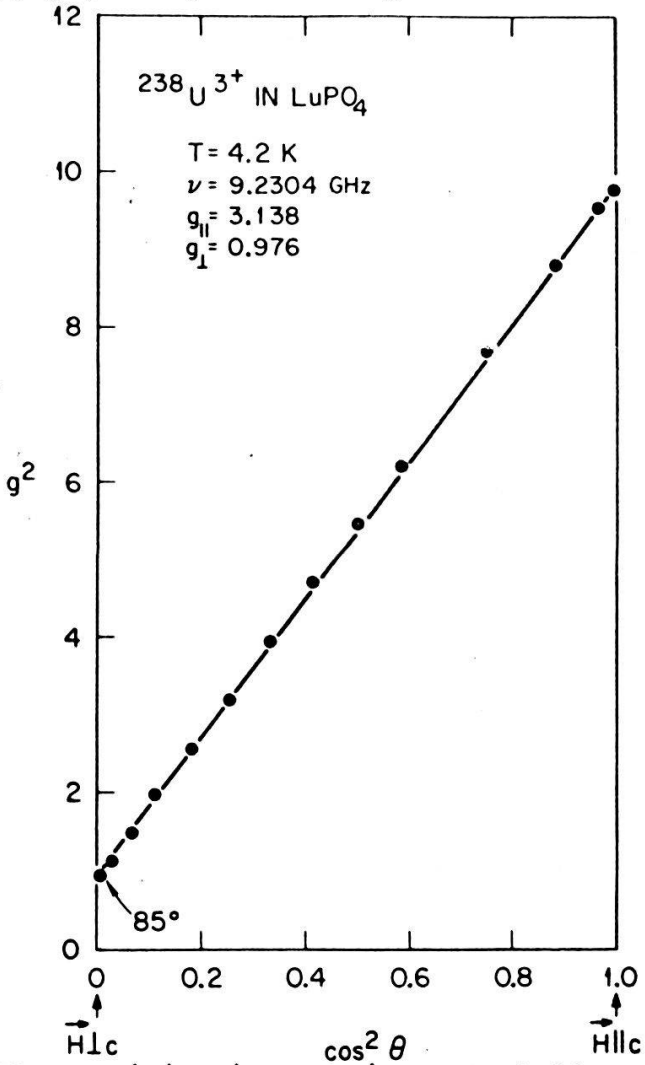

Fig. 12. Position of the U^{3+} EPR transition in xenotime-type $LuPO_4$. The square of the g-value is plotted versus $\cos^2\theta$, where θ is the angle between $\vec{H}$ and the c-axis.

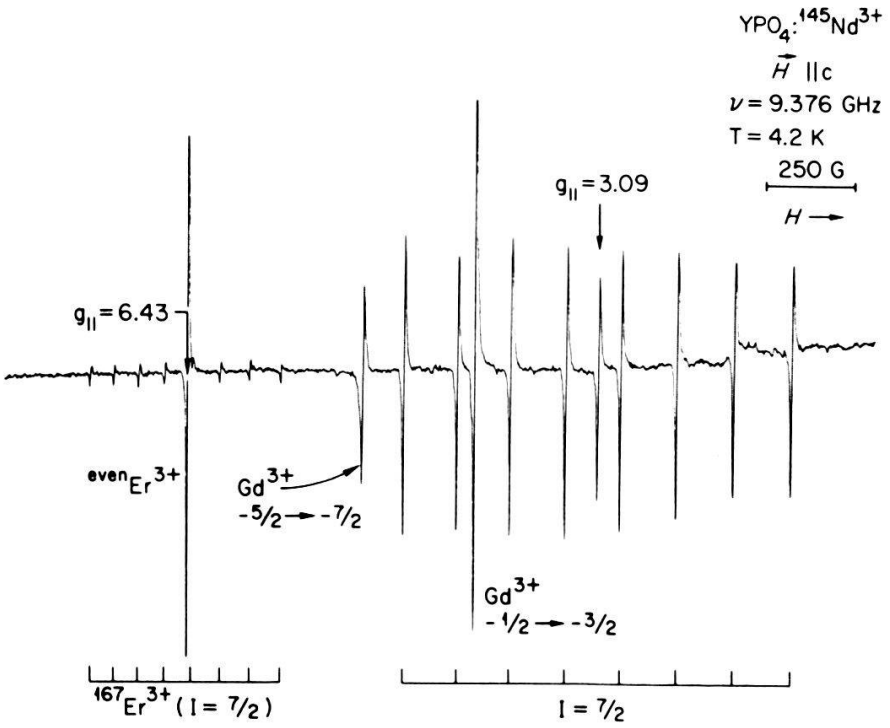

Fig. 13. EPR spectrum of enriched $^{145}Nd^{3+}$ isotopes in xenotime single-crystal. The 8 hyperfine lines corresponding to the various values of M_I (I = 7/2) are almost centered around the central g = 3.09 line of the even isotopes. Additional lines of Gd^{3+} and Er^{3+} are also labeled.

The spectrum of $^{145}Nd^{3+}$ ($4f^3$, $^4I_{9/2}$) is given in Fig. 13. (Lines due to unintentional Er^{3+} impurities are also present). The 8 hyperfine lines due to the I = 7/2 nuclear momentum of ^{145}Nd clearly identifies this impurity and also provides a g-value very close to that observed for the isoelectronic $5f^3$ U^{3+} impurity (see Fig. 12). This permits to interpret the single line measured in Fig. 12 as effectively due to ^{238}U. (Depleted Uranium which is the only one readily available on the market has no nuclear magnetic moment).

5. CONCLUSION

The type of information that can be obtained by means of EPR spectroscopy is summarized in Fig. 14. The number and magnetic-field position of EPR lines reflect the type of impurity being studied, the valence state of this impurity and the local crystal-field symmetry at the impurity site.

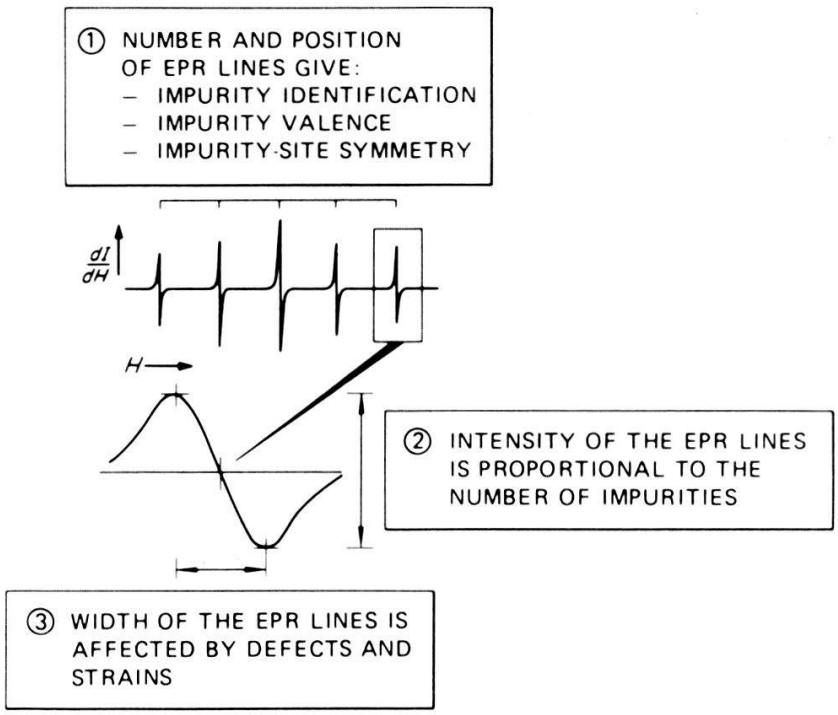

Fig. 14. The type of information provided by EPR.

The basic formalism which is used to interpret such measurements has been given in section 3 while a few examples were presented in the following section. The application of EPR to waste form characterization emphasized studies of lanthanide orthophosphates but the same technique has been successfully applied to many other solid-state problems.

In addition to the information noted above, EPR can also be used to obtain quantitative analytical results. It should be kept in mind, however, that line intensity measurements have to be correlated to those impurities which are in the proper valence state and crystallographic site and not necessarily to the overall impurity concentration. Finally, information concerning imperfections in the host material (e.g. radiation-induced defects, strains, etc.) may be estimated from the EPR linewidths.

REFERENCES

1 G. E. Pake and T. L. Estle, The Physical Principles of Electron Paramagnetic Resonance, W. A. Benjamin Inc. Pub. (1973).

2 J. W. Orton, Electron Paramagnetic Resonance, Gordon & Breach (1968).

3 W. Low, Paramagnetic Resonance in Solids, Academic Press, New York (1960), suppl. 2 of Solid State Physics.

4 C. P. Slichter, Principles of Magnetic Resonance, Springer Verlag (1978).

5 J. E. Harriman, Theoretical Foundations of Electron Spin Resonance, Academic Press (1978).

6 R. S. Alger, Electron Paramagnetic Resonance (Techniques and Applications), Interscience Pub., New York (1968).

7 C. P. Poole, Jr., Electron Spin Resonance, A Comprehensive Treatise on Experimental Techniques, Interscience, New York (1967).

8 A. Abragam and B. Bleaney, Electron Paramagnetic Resonance of Transition Ions, Clarendon Press, Oxford (1970).

9 Nuclear and Electron Resonance Spectroscopies Applied to Materials Science, Eds. E. N. Kaufman and G. K. Shenoy, Proceedings of the MRS meeting 1980, Boston, 1980, North Holland (1981).

10 J. J. van der Klink, this proceeding.

11 Alternate Nuclear Waste Forms and Interactions in Geologic Media, Conf. Proc. 8005107, Eds. L. A. Boatner and C. C. Battle, Jr., U. S. DOE, Washington D.C. (1981).

12 S. A. Al'tshuler and B. M. Kozyrev, Electron Paramagnetic Resonance, Academic Press, New York (1964).

13 L. A. Boatner, G. W. Beall, M. M. Abraham, C. B. Finch, P. G. Huray and M. Rappaz, in Scientific Basis for Nuclear Waste Management, Ed. C. J. Northrup, Plenum Press, New York, (1980), Vol. II, p. 289.

14 M. M. Abraham, L. A. Boatner and M. Rappaz, Phys. Rev. Lett. 45 (10), 839 (1980).

15 M. Rappaz, J. O. Ramey, L. A. Boatner, J. Chem. Phys. 76 (1), 40 (1982).

16 M. M. Abraham, L. A. Boatner, T. C. Quinby, D. K. Thomas and M. Rappaz, Radioactive Waste Management 1, 181 (1980).

17 M. Rappaz, L. A. Boatner and M. M. Abraham, J. Chem. Phys. 73 (3), 1095 (1980).

18 M. Rappaz, M. M. Abraham, J. O. Ramey and L. A. Boatner, Phys. Rev. 23 (3), 1012 (1981).

19 M. M. Abraham, L. A. Boatner and M. Rappaz, to be published.

20 M. M. Abraham, L. A. Boatner, J. O. Ramey and M. Rappaz, J. Chem. Phys. 78 (1), 3 (1983).

21 M. M. Abraham, L. A. Boatner and M. Rappaz, Asilomar Conf. Grounds, California (1981).